AIAA AVIATION Forum
June 25-29, 2018, Atlanta, Georgia
2018 Flow Control Conference

10.2514/6.2018-3376

Transonic Super-critical Airfoil Enhancement by Coflow Jet Downstream of Normal Shock

Michael G. Fernandez,* Jonathan N. Hoffmann,*
Ge-Cheng Zha†
Department of Mechanical and Aerospace Engineering
University of Miami, Coral Gables, Florida 33124
E-mail: gzha@miami.edu

This paper performs a numerical study to enhance transonic supercritical Coflow Jet (CFJ) airfoil cruise performance by placing the CFJ downstream of the normal shock wave. The Reynolds averaged Navier-Stokes(RANS) equations with one-equation Spalart-Allmaras turbulence model is used. A 3rd order weighted essentially non-oscillatory (WENO) scheme with a low diffusion Riemann solver is utilized to evaluate the inviscid fluxes. A 2nd order central differencing scheme is employed for the viscous terms. Numerical trade studies are carried out to investigate CFJ location effects on the shock location and the airfoil efficiency enhancement. This research discovers that placing a CFJ downstream of a shock wave, results in an induction effect that moves the shock further downstream with enlarged supersonic region. Furthermore, the CFJ placed downstream of the shock wave will not suffer the entropy increase due to the shock boundary interaction occurring between the CFJ injection and suction. It substantially reduces the CFJ power expenditure. The effects enhance the cruise efficiency of the supercritical airfoil for both the coefficient of lift C_L and the aerodynamic efficiency $(\frac{L}{D})_c$, which takes into consideration the power required to run the CFJ. The study shows that the aerodynamic efficiency is increased by 5.26% over the baseline RAE2822 and decreasd by 6.68% over the standard CFJ-RAE2822. Measuring by peak $(C_L^2/C_D)_c$ results in an efficiency increase of 6.68% over the baseline RAE2822 and a decrease of 17.51% over standard CFJ-RAE2822.

Nomenclature

AoA	Angle of Attack
CFJ	Co-Flow Jet
LE	Leading Edge
TE	Trailing Edge
$RANS$	Reynolds-Averaged Navier-Stokes
$ZNMF$	Zero-Net Mass Flux
V	Flow Velocity
ρ	Air Density
$\dot{m}$	Mass Flow Rate
M_i	Isentropic Mach Number
R_e	Reynolds Number
L	Aerodynamic Lift
D	Aerodynamic Drag
p	Static Pressure
p_0	Total Pressure
P	Co-Flow Jet Required Pumping Power

*Undergraduate Research Assistant and AIAA Student Member.
†Professor, Director of the Computational Fluid Dynamics and Aerodynamics Laboratory, and AIAA Associate Fellow.

η	CFJ Pumping System Efficiency
q_∞	Freestream Dynamic Head
C_L	Lift Coefficient
C_D	Drag Coefficient
C_M	Moment Coefficient
C_p	Pressure Coefficient
C_μ	Jet Momentum Coefficient
L/D	Conventional Aerodynamic Efficiency
P_c	Co-Flow Jet Pumping Power Coefficient
$(L/D)_c$	Corrected Aerodynamic Efficiency for CFJ Airfoil
(C_L^2/C_D)	Productivity Efficiency Coefficient
$(C_L^2/C_D)_c$	Productivity Efficiency Coefficient correct for the CFJ airfoil
R	Aircraft range
$\bar{W}$	The averaged weight of the aircraft during cruise
γ	Air specific heat ratio
H_t	Total specific enthalpy
T_t	Total temperature
P_t	Total pressure
S	Platform area of the wing
α	Angle of Attack
∞	Subscript, stands for Free Stream Conditions
$_j$	Subscript, stands for Jet Coniditions
$_c$	Subscript, stands for corrected

I. Introduction

I.A. Background

I.B. CFJ Active Flow Control

A CFJ airfoil is a zero-net mass-flux (ZNMF) active flow control technique developed by Zha et al.,[2–13] which achieves radical airfoil lift augmentation, drag reduction, and stall margin increment at low energy expenditure.

In the CFJ airfoil concept, an injection slot near leading edge and a suction slot near trailing edge on the airfoil suction surface are created as sketched in Figure 1. A small amount of mass flow is withdrawn into the airfoil near the trailing edge (TE), pressurized and energized by a pumping system inside the airfoil, and then injected near the leading edge (LE) in the direction tangent to the main flow. The whole process does not add any mass flow to the system and hence is a ZNMF flow control.

The CFJ airfoil flow process provides a unique low energy expenditure mechanism, which has the injection near the suction peak of the airfoil where the lowest main flow pressure is located, and jet suction located near trailing edge where the highest main flow pressure is located. In other words, the required pumping energy is low since the low pressure makes the jet easy to be ejected out and high pressure makes the jet easy to be sucked in. The required pumping work of CFJ airfoil would be lower than those of the flow control methods injecting near trailing edge such as a CC airfoil. Dano et al.[9,10] investigate the energy expenditure of the CFJ airfoil, which indicates that the CFJ airfoil gains more performance enhancement at higher angle of attack(AoA) due to lower energy expenditure. As pointed out by Zha et al.,[5] the injection and suction of CFJ airfoil are efficiently integrated and they both enhance boundary layer momentum and airfoil circulation.

The fundamental mechanism of CFJ airfoil is that the turbulent mixing between the jet and main flow makes a lateral transport of energy between the jet, boundary layer, and main flow to energize the wall boundary layer. The large vortex structures and adverse pressure gradient are all beneficial to enhance mixing. The energized boundary layer drastically increases the circulation, augments lift, and reduces the total drag or generates thrust(net negative drag). While the earliest studies of the CFJ focused on the subsonic flow

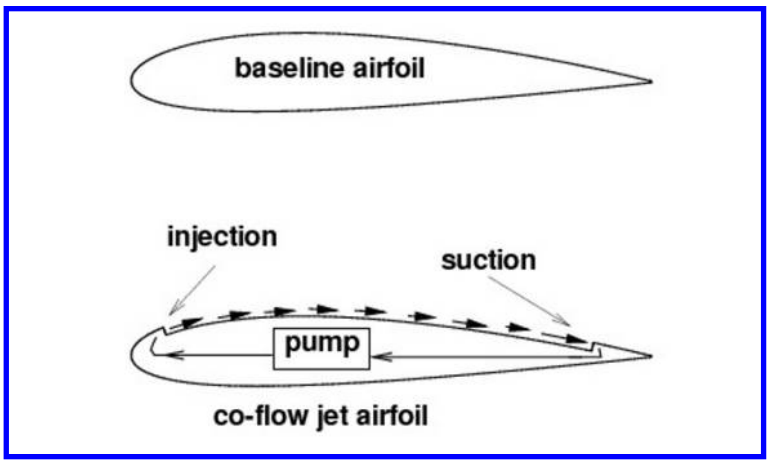

Figure 1. The sketch of a baseline airfoil and a CFJ airfoil.

regime, Liu and Zha[1] further proved that the performance of the CFJ penetrates into the transonic realm as well. With the standard CFJ implementation previously described, Liu and Zha's[1] study of the transonic CFJ performance found that, at peak efficiency, the CFJ achieves a simultaneous increase of C_L and $(\frac{L}{D})_c$ over a baseline RAE2822 airfoil of 18.7% and 14.5%, respectively.[2]

The purpose of this study is to improve on the previously demonstrated capabilities of CFJ airfoil in transonic flow regime by placing the CFJ down stream of the shock wave and to further understand the relationship between shock waves and the CFJ. It is hoped that this research will pave the way for further research and progress into understanding and improving the performance of the CFJ in transonic and supersonic Mach regimes.

II. Methodology

II.A. Numerical Approach

The in-house computational fluid dynamics (CFD) code Flow-Acoustics-Structure Interaction Package (FASIP) is applied to conduct the numerical simulations. The Reynolds averaged Navier-Stokes (RANS) equations with one-equation Spalart-Allmaras (SA)[14] turbulence model is used for this research. The low diffusion E-CUSP scheme suggested by Zha et al.[13] and Roes flux difference scheme[15] with the 5th order weighted essentially non-oscillatory (WENO) scheme proposed by Shen et al[16] are utilized to evaluate the inviscid fluxes. The 4th order central differencing method suggested by Shen et al.[17] is used for the viscous terms descritization. The implicit Gauss-Seidel (GS) line relaxation with two alternative sweeping direction in each time step is applied to achieve a fast convergence rate.[18] Parallel computing is implemented to save wall clock simulation time.[19] The code is extensively validated with various transonic flows including CFJ airfoil flows.[7,10,19–23]

II.B. CFJ Airfoil Parameters

II.B.1. Drag and Lift

The momentum exchange and pressure difference at the injection and suction slots produce reactionary force to the airfoil, which contribute to the total drag and lift. Through control volume analysis, Zha et al.[6] give the following formulations to calculate the lift and drag due to CFJ effect for CFD simulation

$$R_x = (\dot{m}_j V_{j1} + p_{j1} A_{j1})\ cos(\theta_1 - \alpha) - (\dot{m}_j V_{j2} + p_{j2} A_{j2})\ cos(\theta_2 + \alpha) \quad (1)$$

$$R_y = (\dot{m}_{j1}V_{j1} + p_{j1}A_{j1})\ sin(\theta_1 - \alpha) + (\dot{m}_{j2}V_{j2} + p_{j2}A_{j2})\ sin(\theta_2 + \alpha) \tag{2}$$

where x and y represent the drag and lift direction respectively, subscripts 1 and 2 stand for the injection and suction, θ_i (i = 1,2) is the angle between the injection or suction slot surface and the line normal to the airfoil chord, and is the AoA, as shown in Figure 2.

The total drag and lift of the CFJ airfoil can then be expressed as:

$$D = F_x - R_x \tag{3}$$

$$L = F_y - R_y \tag{4}$$

where F_x and F_y are the drag and lift force due to surface integral of pressure and shear stress. The corresponding drag and lift coefficients are expressed as following

$$C_D = \frac{D}{\frac{1}{2}\rho_\infty {V_\infty}^2 S} \tag{5}$$

$$C_L = \frac{L}{\frac{1}{2}\rho_\infty {V_\infty}^2 S} \tag{6}$$

where ρ_∞ and V_∞ denote the free stream density and velocity. S is the wing planform area.for 2-D airfoil studies, S denotes the planform area per unit span, which is equal to the airfoil chord length.

II.B.2. Jet Momentum

The jet momentum coefficient C_μ is a parameter used to quantify the jet intensity, which is defined as

$$C_\mu = \frac{\dot{m}V_j}{\frac{1}{2}\rho_\infty {V_\infty}^2 S} \tag{7}$$

where $\dot{m}$ is the injection mass flow rate, V_j is the averaged injection velocity at the injection slot opening.

II.B.3. Power Consumption

The CFJ can be implemented by mounting a pumping system inside the wing that withdraws air from the suction slot and blows it into the injection slot. The power consumption can be determined by the jet mass flow and total enthalpy change as following

$$P = \dot{m}(H_{01} - H_{02}) \tag{8}$$

where H_{01} and H_{02} are the total enthalpy in the injection cavity and suction cavity, respectively. P is the power required by the pump. Introducing the pump efficiency η and total pressure ratio of the pump $\Gamma = \frac{P_{01}}{P_{02}}$, the power consumption can be expressed as

$$P = \frac{\dot{m}C_pT_{02}}{\eta}(\Gamma^{\frac{\gamma-1}{\gamma}} - 1) \tag{9}$$

where γ is the specific heat ratio for air. The power consumption can be further normalized as a power coefficient as below

$$P_c = \frac{P}{\frac{1}{2}\rho_\infty V_\infty^3 S} \tag{10}$$

II.B.4. Aerodynamic Efficiency

The conventional airfoil aerodynamic efficiency is defined as

$$(\frac{L}{D}) = \frac{C_L}{C_D} \tag{11}$$

For the CFJ airfoil, the ratio above represents the pure aerodynamic relationship between lift and drag. To take account of the energy consumption of the CFJ, the conventional aerodynamic efficiency is modified by converting the power consumption into a corresponding drag force. The equation of the corrected aerodynamic efficiency is given as following[10]

$$(\frac{L}{D})_c = \frac{L}{D + \frac{P}{V_\infty}} \tag{12}$$

in which the pump power consumption P is converted into a force $\frac{P}{V_\infty}$ added to the aerodynamic drag D. The formulation above can be further expressed using the non-dimensional coefficients C_L, C_D and P_c as

$$(\frac{L}{D})_c = \frac{C_L}{C_D + P_c} \tag{13}$$

Note that when the pumping power is set to 0, $(\frac{L}{D})_c$ returns to conventional aerodynamic efficiency definition.

II.B.5. Aircraft Productivity

The new term of "productivity coefficient" is raised to represent the transportation ability of an aircraft by combing the total aircraft weight and the maximum range.[1]

For a jet engine airplane, the total weight of the aircraft decreases during flight. A non-dimensional productivity parameter is hence defined using the aircraft averaged weight as below.

$$C_{RW} = \frac{R\bar{W}}{\frac{1}{2c_t}\bar{\rho}V_\infty^3 S} = \eta\frac{C_L^2}{C_D} ln\frac{W_0}{W_f} \tag{14}$$

where R is the aircraft range, $\bar{W}$ is the averaged weight of the aircraft during cruise, c_t is the engine cruise thrust specific fuel consumption [fuel weight[N]/(thrust(N) s)], $\bar{\rho}$ is the averaged air density due to altitude variation during cruise, S is the wing platform area, W_0 is the aircraft initial gross weight at takeoff, W_f is the final weight at landing. This formulation is obtained from the Breguet Range Equation. The productivity parameter represents the productivity of the aircraft with the fuel consumed per unit time.

To compare aircraft that have the same ratio of initial weight to final weight with the same engine fuel consumption, the only factor affecting their productivity parameter is C_L^2/C_D. We hence name C_L^2/C_D as

productivity efficiency.

We consider the productivity efficiency $C_L^2/C_D = C_L(C_L/C_D)$ as a more comprehensive parameter than the conventional aerodynamic efficiency C_L/C_D to measure the merit of an airplane aerodynamic design for cruise performance. The former includes not only the information of C_L/C_D, but also the information of the aircraft weight C_L. For example, for two airplane designs having the same C_L/C_D with one C_L twice as large as the other, if the wing sizes are the same, one airplane will be able to carry twice as much weight than the other with the productivity and wing loading increased by 100%. Such a large difference is not reflected by C_L/C_D, but very well reflected by C_L^2/C_D.

The definition of C_L/C_D in general is a suitable measure of merit for conventional aircraft design. This is because at certain Mach number regimes, the maximum C_L/C_D is usually achieved at low angle of attack within the drag bucket and is more or less the same for different airfoil designs. In other words, for the same optimum C_L/C_D, the C_L is about the same. A typical C_L for subsonic airfoil is about 0.4 and for transonic airfoil is about 0.7.

III. CFD Simulation Setup

III.A. CFD Code

The in-houes FASIP (Flow-Acoustics-Structure Interaction Package) CFD code is used to conduct the numerical simulation. The 2D Reynolds averaged Navier-Stokes (RANS) equations with one-equation Spalart-Allmaras[16,17] turbulence model is used. A 3^{rd} order WENO scheme for the inviscid flux and a 2^{nd} order central differencing for the viscous terms are employed to discretize the Navier-Stokes equations. The RANS solver is validated for CFJ airfoil simulations.[2,7,9]

III.B. Boundary Conditions

The 3^{rd} order accuracy no slip condition is enforced on the solid surface with the wall treatment to achieve the flux conservation on the wall.[16] Total pressure, total temperature, and flow angles are specified as the inlet boundary conditions for the upstream portion of the farfield boundary and inside the injection cavity. Constant static pressure is used for the downstream farfield boundary and inside the suction cavity.

III.C. C_μ Iteration

To achieve zero net mass flux with the CFJ flow control, the mass flow exiting the injection slot must be equal to the mass flow entering the suction slot, i.e. $\dot{m}_{inj} = \dot{m}_{suc}$. The prescribed jet momentum coefficient C_μ is achieved by adjusting the injection cavity total pressure. Total temperature is assumed constant during this process. The injection and suction mass flow rates are matched by adjusting the suction cavity statis pressure. The iterative process is conducted throughout the simulation until the specified momentum coefficient is reached and the injection and suction mass flow match within the acceptable tolerance, which is 0.2% for the present study.

IV. Structure of the Trade Study

IV.A. Baseline Comparisons

Both the supercritical RAE2822 and CFJ-RAE2822 airfoils are chosen for baseline comparisons. The RAE2822 supercritical airfoil has the maximum thickness of 12.1% at 37.9% chord and maximum camber of 1.3% at 75.7% chord. The computational parameters are selected based on the numerical simulations in Liu and Zha's transonic study,[2] which is further based on the AGARD report,[25] and has the freestream conditions of Re_∞=6.5 $\times 10^6$ and $M_\infty = 0.729$. O-type structured grids are utilized for the study. The Aft-CFJ-RAE2822 study begins with the freestream conditions previously mentioned, as well as the angle of attack ($\alpha = 2.31°$) that is used in the AGARD report.

As this is the first study ever performed with the CFJ injection slot located downstream of the shock wave, the initial geometric characteristics are generally based on Liu and Zha's transonic CFJ study.[2] As such, the only variables investigated in the trade study are those that have made the most significant differences in efficiency for the previous CFJ airfoil studies, the injection slot location, the injection slot width, and the C_μ.[4,2]

The study is broken down into five phases. Phase one is a proof of concept utilizing coarse meshes which studies the injection slot width. Phase two is a mesh refinement study utilizing only the peak efficiency injection slot width discovered in phase one. Phase three is a trade study between the C_μ and injection slot location utilizing the refined mesh. Phase four is an AoA and C_μ trade study between the peak Aft-CFJ-RAE2822 efficiency configurations. Phase five finishes off the study with an isolated trend analysis through a small trade study containing AoA, C_μ, and injection slot location.

IV.A.1. CFJ Injection Slot

The injection slot location chosen for the proof of concept is 63%c and is studied with four different injection slot widths: 0.11%c, 0.13%c, 0.15%c, and 0.17%c; all at a C_μ of 0.0025 . For the trade study, following the mesh refinement study, injection slot location studied ranges from 61%c to 65%c. To optimize the system for efficiency, two injection slot locations are added on either side of the peak location discovered in the initial trade study. Figure 2 displays the five different injection slot locations superimposed into a single image. Figure 3 displays the injection slot widths studied during phase one.

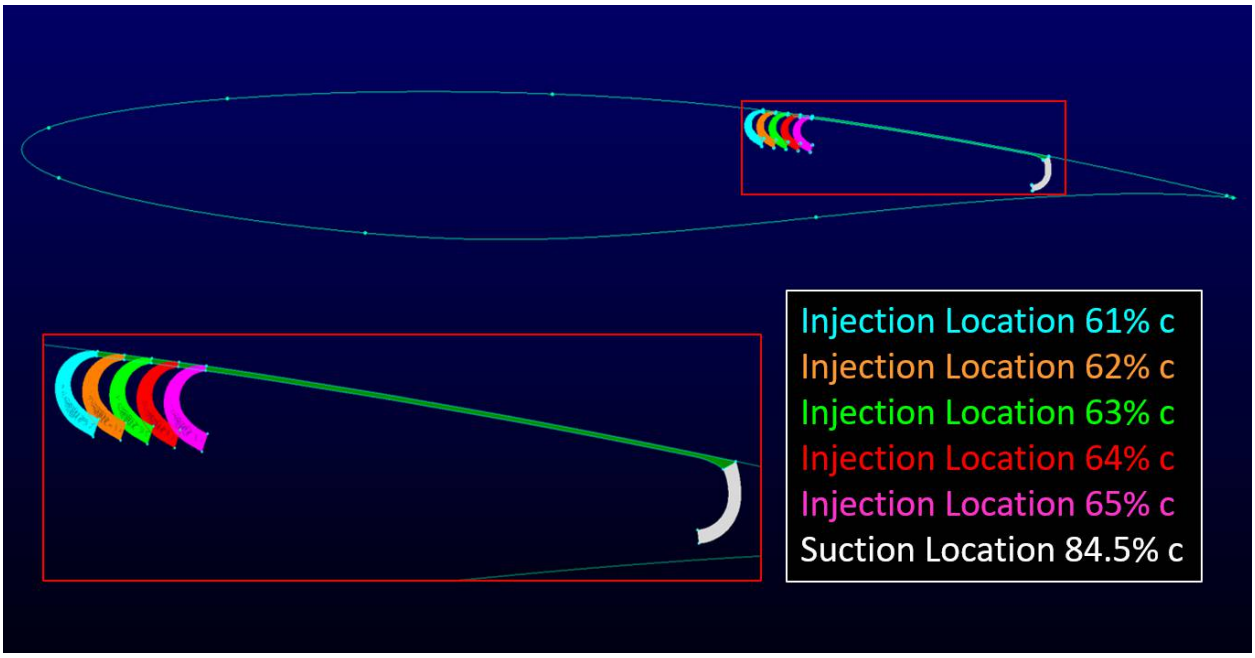

Figure 2. Aft-CFJ RAE2822 Phase one injection location variation along chord

IV.A.2. Coefficient of Mass Flow Rate (C_μ)

During phase one of the study, a single value of 0.0025 C_μ is studied. During the trade study in phase three, C_μ ranges from 0.00175 to 0.00275. Similar to the injection slot location study, a C_μ data point is added on either side of peak location discovered, resulting in two additional C_μ data points of 0.00187 and 0.00212.

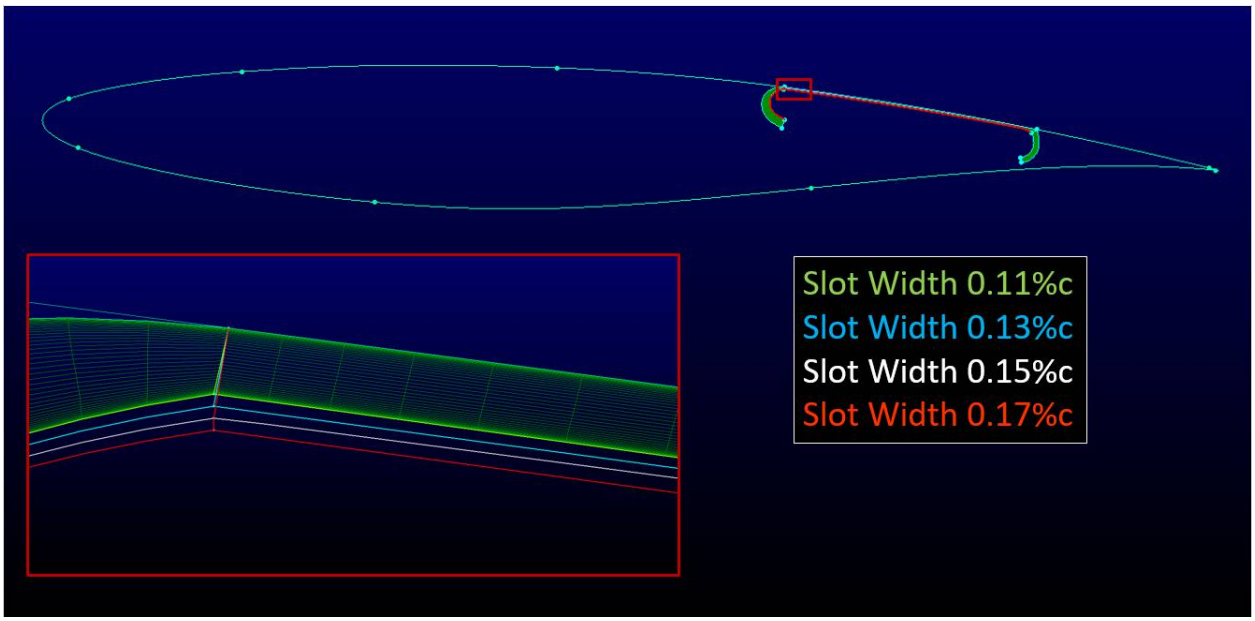

Figure 3. Aft-CFJ RAE2822 Phase one injection slot width variation at 0.63 c

IV.A.3. Mesh

Phase one of the trade study has an outer region mesh consisting of 631 x 77 cells, along with CFJ region of the mesh which contains 158 x 45 cells. This totals to 54,788 cells with a wall spacing of $4x10^{-6}$. Phase two, the mesh refinement study, evaluates the peak performance configuration with a mesh size of 1272 x 77 and 1272 x 150. The mesh was refined further to dimensions of 1272 x 228 and 1913 x 228, equaling 290,016 cells and 436,164 cells, respectively. The mesh refinement study demonstrates convergence with the mesh dimensions of 1272 x 151 cells in the outer region, with 318 x 90 cells in the CFJ region. The totals come out to 192,072 and 28,620 cells, respectively, with a wall spacing of $4x10^{-6}$.

IV.A.4. Angle of Attack (AoA, α)

Angle of attack is studied during phase four of the trade study. AoA increments of 1° were used from 1°-5°, but smaller increments were used near AoA 2° due to results of previous RAE2822 and CFJ-RAE2822 studies. The AoA study includes 1.8°, 1.9°, 2°, 2.1°, and 2.2°. Table 1 displays a summarized outline of the full trade study. During the AoA study, C_μ ranges from 0.00175 to 0.0025.

V. Results and Analysis

V.A. Phase One: Coarse Mesh Trade Study

V.A.1. Injection Slot Location

Placing the CFJ aft of the normal shock strengthens the shock wave, decreasing the pressure behind the shock and moves the shock further downstream by 0.05c with enlarged supersonic region. Figures 4 and 5 display the flow field of the baseline RAE2822 and the standard CFJ-RAE2822. Figure 6 is the Mach contour of the Aft-CFJ with an injection slot width 0.15%c and an injection slot location of 0.63c. In comparison to the baseline RAE2822, the shock wave location moves down stream by approximately 0.05%c with the addition of the Aft-CFJ.

Phase	Variable	Margins	Increments
One	Injection Slot Width	0.11% c - 0.17% c	0.02% c
	Injection Location	63% c	N/A
	Mass Flow (C_μ)	0.0025	N/A
	Mesh (Outer)	631 x 77	N/A
	Mesh (CFJ)	158 x 45	N/A
Two	Mesh Refinement 1 (Outer)	1272 x 77	N/A
	Mesh Refinement 1 (CFJ)	318 x 45	N/A
	Mesh Refinement 2 (Outer)	1272 x 150	N/A
	Mesh Refinement 2 (CFJ)	318 x 90	N/A
Three	Injection Location	61% c - 65% c	1% c
	Mass Flow (C_μ)	0.00175 - 0.00275	0.00025
Four	Angle of Attack	1° - 5°	1°
	Refined Angle of Attack	1.8° - 2.2°	0.1°
	Mass Flow (C_μ)	0.00175 - 0.0025	0.00025
Five	Angle of Attack	1.8° - 2°	0.1°
	Mass Flow (C_μ)	0.002 - 0.0025	0.00025
	Injection Location	66%c - 67%c	1%c

Table 1. Trade Study Summary

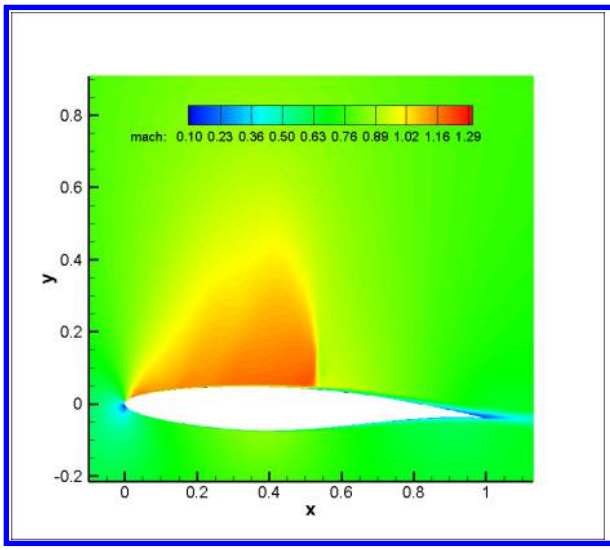

Figure 4. Baseline RAE2822

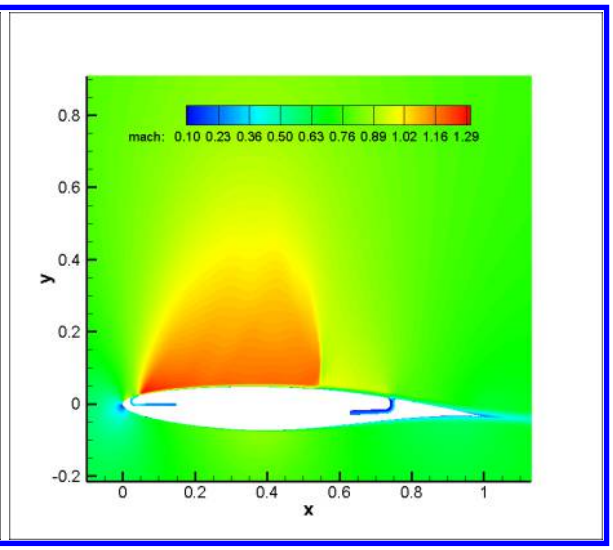

Figure 5. Standard CFJ-RAE2822

V.A.2. Injection Slot Width and Mass Flow

As previous studies have shown, the aerodynamic efficiency decreases as the flow exiting the jet experiences supersonic jet velocities. With supersonic jet velocities, the total pressure in the injection slot is much higher than the total pressure inside of the suction slot, resulting in large values of the power coefficient. Due to the inverse relationship between the $(\frac{L}{D})_c$ and P_c, increasing the injection slot width, which reduces the velocity of the jet, tends to increase the efficiency of the system up to a certain point.

Supersonic jet velocities appear near injection slot 0.13% as can be seen in figures 7 - 10, which display the jet streams out of the injection slots of cases with slot widths 0.11%c - 0.17%c. The benefit of increasing the injection slot width is highly reduced after slot width 0.15%c. So, the study continued with injection slot width 0.15%c.

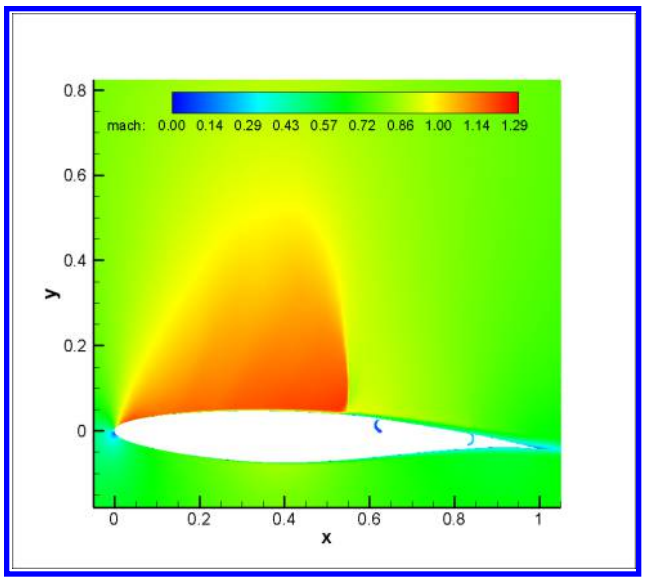

Figure 6. Inj. Slot Width 0.15% c, Location 0.63% c

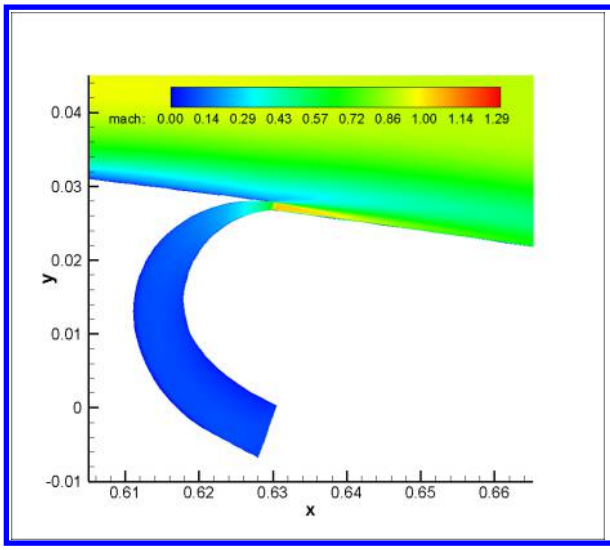

Figure 7. Slot Width 0.11% c

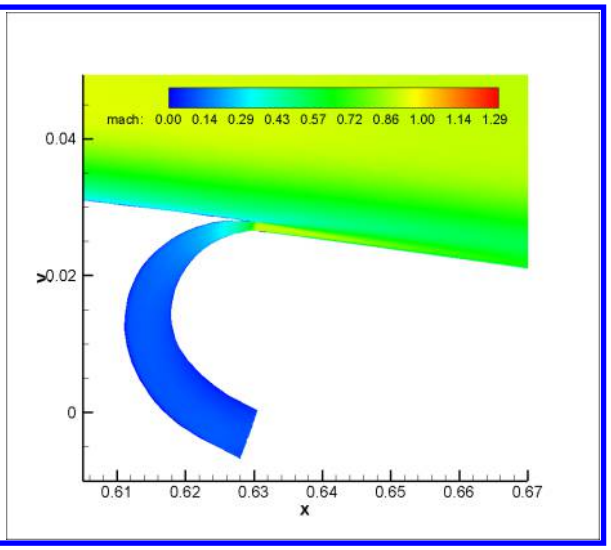

Figure 8. Slot Width 0.13% c

Case	AoA	C_L	C_D	P_c	$(\frac{L}{D})_c$
0.11%	2.31°	0.863761	0.016735	0.0023	45.38
0.13%	2.31°	0.778424	0.012408	0.0014	56.37
0.15%	2.31°	0.771704	0.012578	0.0009	57.26
0.17%	2.31°	0.766711	0.012656	0.0007	57.40

Table 2. Results of the Proof of Concept

As displayed in table 2, the corrected aerodynamic efficiency is nearly the same for injection slot widths 0.15%c and 0.17%c. For the cases with supersonic jet streams, 0.11%c and 0.13%c injection slot widths, the power coefficient largely increases, bringing the corrected aerodynamic efficiency down.

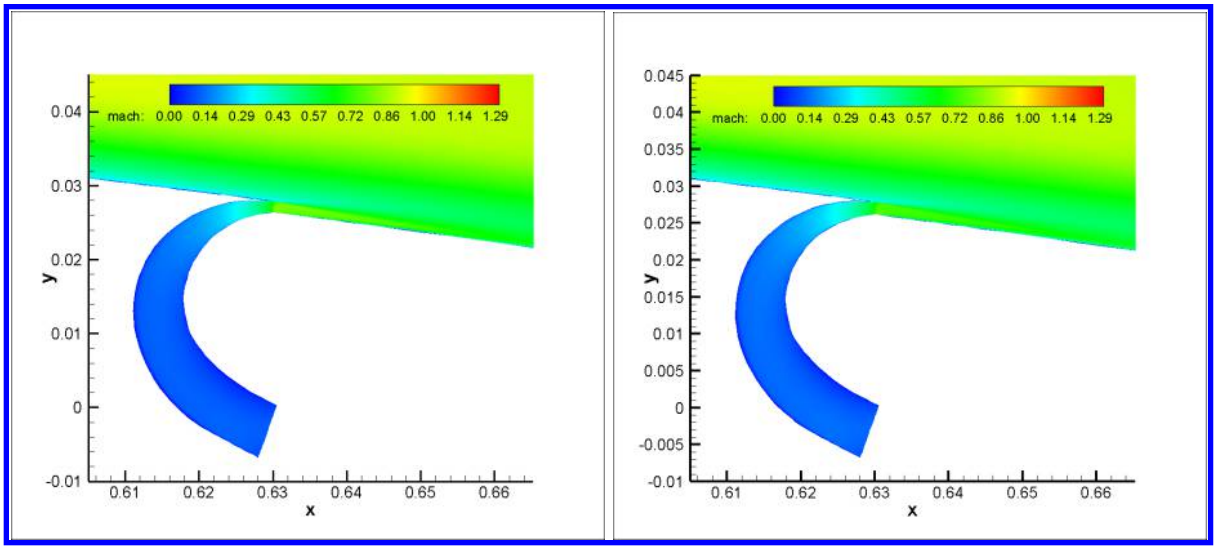

Figure 9. Slot Width 0.15% c

Figure 10. Slot Width 0.17% c

V.B. Phase Two: Mesh Refinement Study

Table 3 demonstrates that the mesh is fully refined with case number 3 of the mesh refinement study. The mesh size from case (1272 x 150) will be used for the remainder of the study.

Case	AoA	Mesh Size	C_L	C_D	P_c
1	2.31°	631 × 77	0.759247	0.011227	0.0010
2	2.31°	1272 × 77	0.749371	0.012127	0.0005
3	2.31°	1272 × 150	0.751679	0.012015	0.0005
4	2.31°	1272 × 228	0.749881	0.011961	0.0005
5	2.31°	1913 × 228	0.750132	0.012002	0.0005

Table 3. Results of Mesh Refinement Study

V.C. Phase Three: Trade Study

Variables studied in phase three include C_μ ranging from 0.00175 to 0.00275 with increments of 0.00025 and injection slot location ranging from 61%c to 65%c with increments of 1%c. To obtain a configuration with greater efficiency, additional data points are added on either side of the discovered peak efficiency locations of the two variables. The data points added are 0.187 and 0.212 for C_μ and 63.5%c and 64.5%c for injection slot location. The results of the study are displayed in figures 7 and 8.

The study shows that increasing the C_μ both increases lift and decreases drag; however, the P_c rises sharply in comparison to the slight decrease in drag, resulting in an ideal C_μ located somewhere in the mid range of the studied values. Figures 9 and 10 display C_D vs C_μ and P_C vs C_μ. The peak efficiency configuration during phase three of the study is found with injection slot location of 64%c and C_μ of 0.00225. The aerodynamic efficiency $(\frac{L}{D})_c$ of this configuration is 54.62.

V.D. Phase Four: Angle of Attack Trade Study

This section performs an AoA study using the previous peak efficiency configuration at 0°, 1°, 1.8°, 1.9°, 2°, 2.1°, 2.2°, 3°, 4°, and 5°. AoA 1.9° and 2° nearly tie for peak efficiency. Results are displayed in Figure 15.

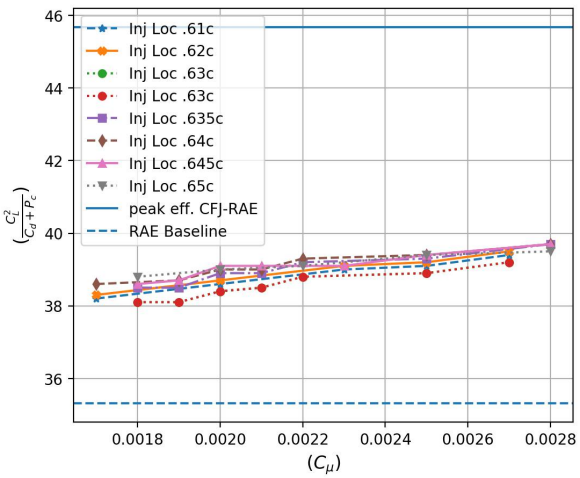

Figure 11. Productivity Efficiency vs C_μ

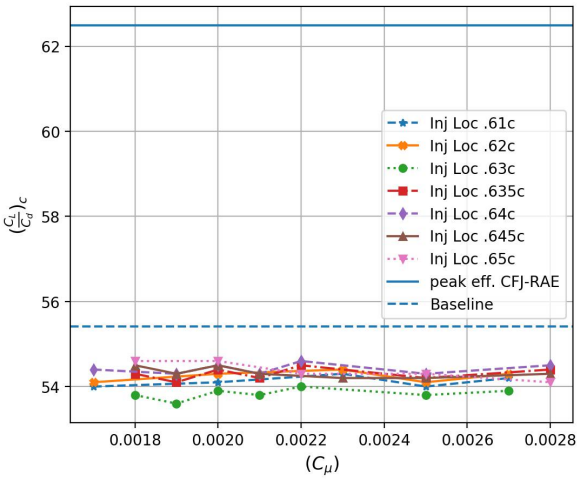

Figure 12. Aerodynamic Efficiency vs C_μ

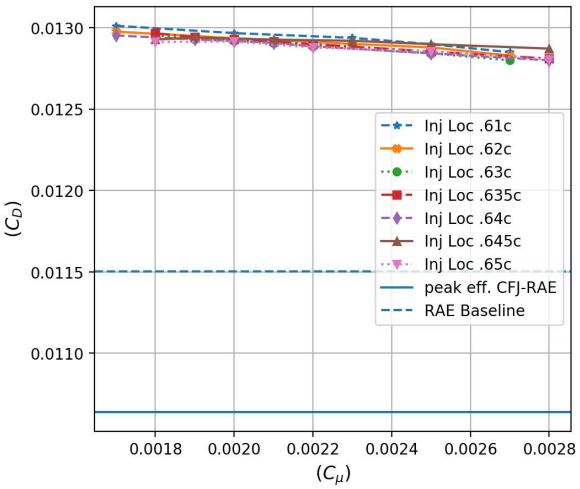

Figure 13. C_D vs C_μ

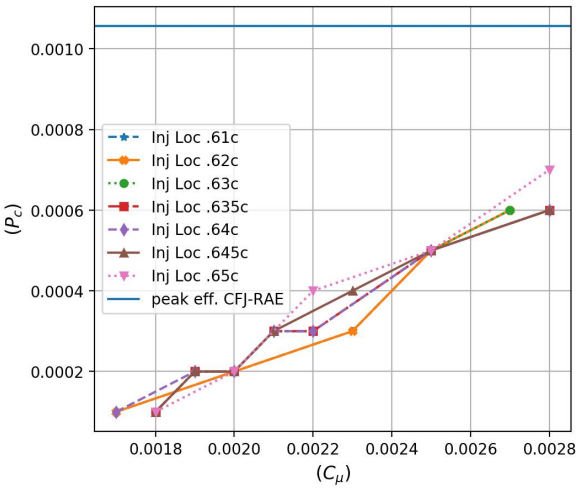

Figure 14. P_c vs C_μ

V.E. Phase Five: Isolated Trend Analysis

The ideal injection slot location is dependent on the location of the shock wave, which changes dramatically with AoA; therefore, a small trade study is performed based on trend analysis of ideal values for each variable studied. The trade study includes injection slot locations of 66% c and 67% c, angles of attack of 1.8°, 1.9°, and 2°, and C_μ of 0.002, 0.00225, and 0.0025.

The final peak efficiency configuration for the Aft-CFJ-RAE2822 is discovered to be injection slot location 67% c, C_μ of 0.0025, and AoA of 1.9°. Results of the trade study may be seen in figure 16 and 17. Overall,the difference in values between AoA 1.8° and 1.9° are rather marginal, with the exception of a single data point where injection location 66%c is substantially lower than injection location 67%c: AoA 2° with C_μ of 0.002.

V.F. Mechanism of CFJ Downstream the Shock

The mechanism to place the CFJ downstream of the terminal normal shock is the following: 1) The CFJ injection creates an induction effect that decrease the pressure behind the shock. Such a lower pressure will decrease the normal shock wave speed that pushes the shock at a further downstream position to match a higher supersonic Mach number. The overall Mach number is hence increased with the supersonic region enlarged as shown in comparing Figures 4 and 6, which results in an increased lift coefficient. Since the

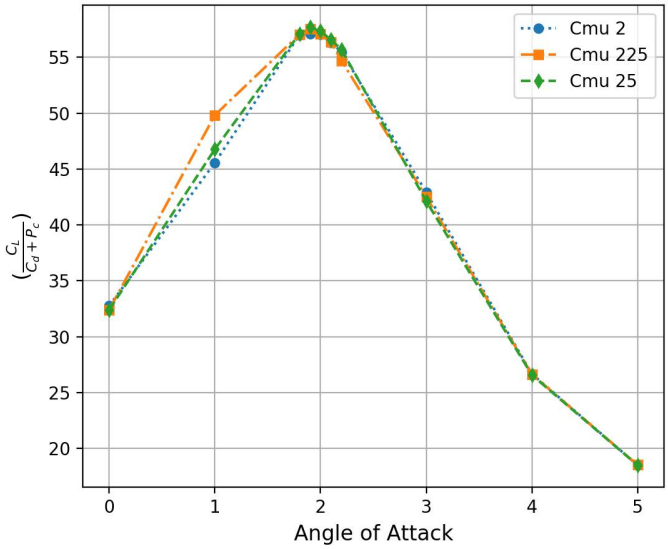

Figure 15. Angle of Attack vs Efficiency

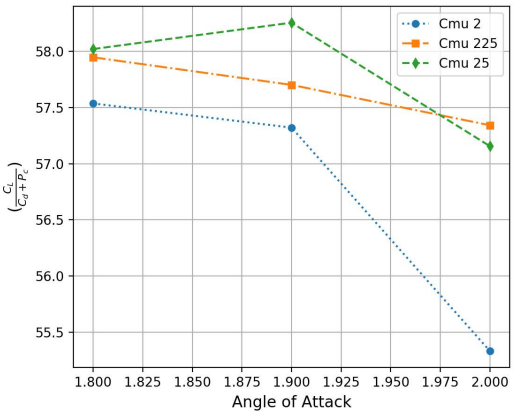

Figure 16. Injection Location 66% c

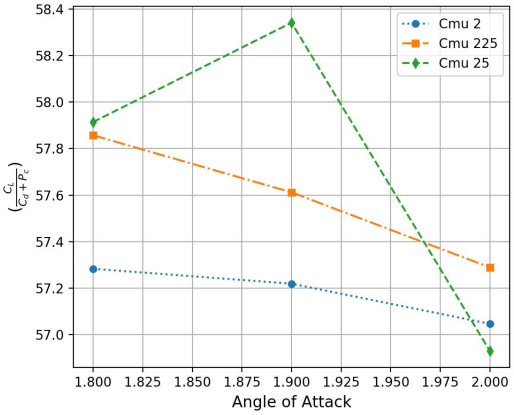

Figure 17. Injection Location 67% c

Mach number increase with the peak Mach number is still less than 1.3 (see Figure 20), the normal shock resembles an isentropic compression wave with low wave drag. 2) The CFJ placed downstream of the shock has an advantage with P_c with no normal shock standing between the injection and suction, which is clearly seen by comparing the P_c of the Aft-CFJ-RAE2822 and the standard CFJ-RAE2822. This brings very low entropy increase and hence requires a CFJ power consumption that is much lower than the standard CFJ as shown in Figure 14. The increased lift coefficient with reduced CFJ power expenditure results in an improved aerodynamic efficiency and productivity efficiency over the baseline RAE2822.

VI. Conclusion

Figure 18 displays the flow field of the peak efficiency configuration. Table 4 displays the tabulated peak efficiency of the Aft-CFJ-RAE2822 against both the baseline RAE2822 and the CFJ-RAE2822. Finally, figures 19 and 20 perform a comparison of the C_p line and isentropic mach number.

Current figures demonstrate that the Aft-CFJ-RAE2822 shows a slight increase in efficiency over the baseline

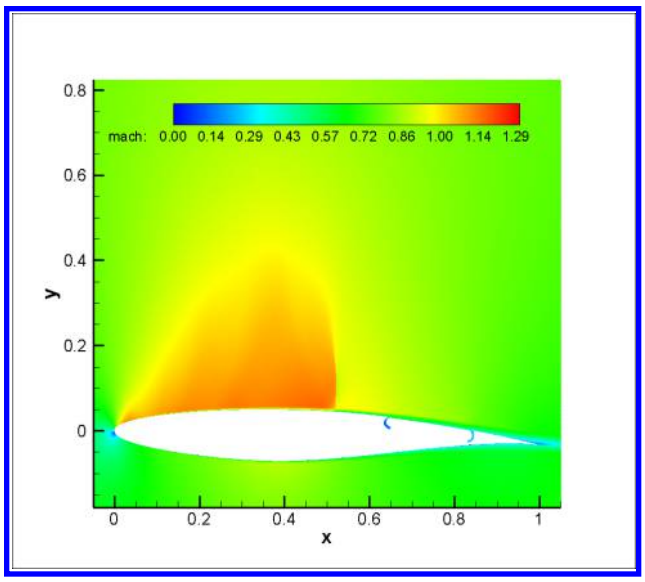

Figure 18. Mach Contour of Peak Efficiency Configuration

RAE2822	AoA	C_L	C_D	P_c	$(C_L/C_D)_c$	$(C_L^2/C_D)_c$
Baseline	2.00°	0.637	0.01150	N/A	55.42	35.32
Standard CFJ	2.00°	0.731	0.01064	0.001	62.49	45.68
Aft-CFJ	1.9°	0.646	0.01067	0.0004	58.34	37.68

Table 4. Tabulated Peak Efficiency Results

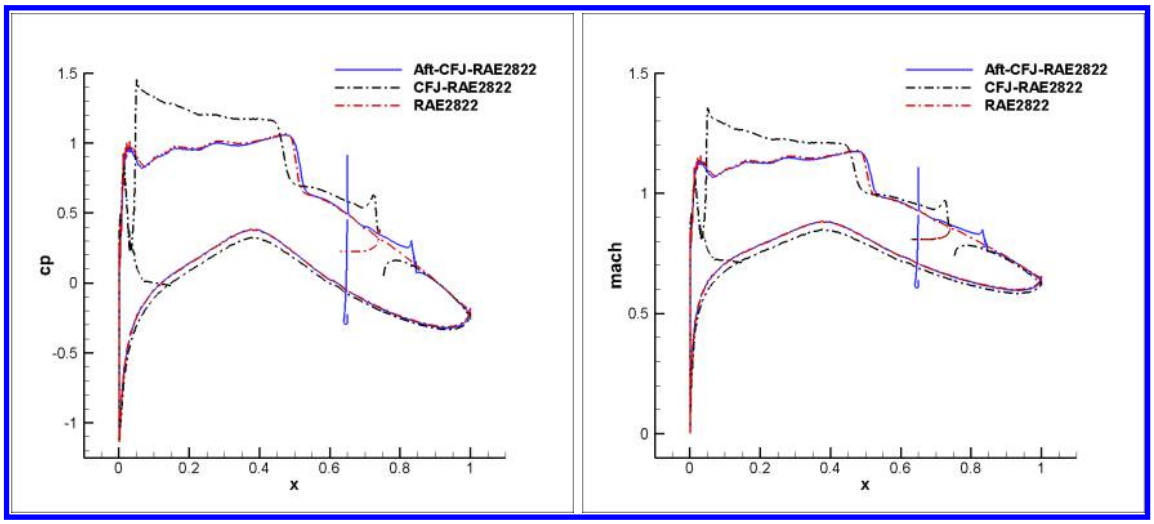

Figure 19. Cp Contour Comparison

Figure 20. Isentropic Mach Number Comparison

RAE2822, but has a decrease in performance over the CFJ-RAE2822. Measuring by peak $(L/D)_c$ results in an efficiency increase of 5.26% over the baseline RAE2822 and a degree of 6.64% over the standard CFJ-RAE2822. Measuring by peak $(C_L^2/C_D)_c$ results in an efficiency increase of 6.68% over the baseline RAE2822 and a decrease of 17.51% over standard CFJ-RAE2822.

Acknowledgments

The authors would like to acknowledge the computing resource provided by the Center of Computational Sciences at the University of Miami.

References

[1]Yunchao Yang and Gecheng Zha, "Super-Lift Coecient of Active Flow Control Airfoil: What is the Limit?." AIAA Paper 2017-1693, AIAA SCITECH2017, 55th AIAA Aerospace Science Meeting, Grapevine, January 9-13 2017.

[2]Z. Liu and G.-C Zha, Transonic Airfoil Performance Enhancement Using Co-Flow Jet Active Flow Control, AIAA Journal, No. 2016.

[3]G.-C. Zha and D. C. Paxton. A Novel Flow Control Method for Airfoil Performance Enhancement Using Co-Flow Jet. Applications of Circulation Control Technologies, Chapter 10, p. 293-314, Vol. 214, Progress in Astronautics and Aeronautics, AIAA Book Series, Editors: Joslin, R. D. and Jones, G.S., 2006.

[4]G.-C Zha and C. Paxton and A. Conley and A. Wells and B. Carroll. Effect of Injection Slot Size on High Performance Co-Flow Jet Airfoil. AIAA Journal, 43, 2006.

[5]G.-C. Zha and W. Gao and C. Paxton. Jet Effects on Co-Flow Jet Airfoil Performance. AIAA Journal, No. 6, 45:12221231, 2007.

[6]G.-C Zha and B. Carroll and C. Paxton and A. Conley and A. Wells. High Performance Airfoil with Co-Flow Jet Flow Control. AIAA Journal, 45, 2007.

[7]Wang, B.-Y. and Haddoukessouni, B. and Levy, J. and Zha, G.-C. Numerical Investigations of Injection Slot Size Effect on the Performance of Co-Flow Jet Airfoil . AIAA Journal of Aircraft, 45:20842091, 2008.

[8]B. P. E. Dano, D. Kirk, and G.-C. Zha. Experimental Investigation of Jet Mixing Mechanism of CoFlow Jet Airfoil. AIAA Paper 2010-4421, 5th AIAA Flow Control Conference, Chicago, IL,, 28 Jun - 1 Jul 2010.

[9]B. P. E. Dano, G.-C. Zha, and M. Castillo. Experimental Study of Co-Flow Jet Airfoil Performance Enhancement Using Micro Discreet Jets. AIAA Paper 2011-0941, 49th AIAA Aerospace Sciences Meeting, Orlando, FL,, 4-7 January 2011.

[10]Lefebvre, A. and Dano, B. and Di Franzo, M. and Bartow, W. and Zha, G.-C. Performance of Co-Flow Jet Flow Airfoil with Variation of Mach Number. AIAA Paper 2013-0490, 51st AIAA Aerospace Science Meeting, Grapevine, TX, 7-10 Jan. 2013, to appear in Journal of Aircraft, 2016.

[11]Lefebvre, A. and Zha, G.-C. Numerical Simulation of Pitching Airfoil Performance Enhancement Using Co-Flow Jet Flow Control. AIAA Paper 2013-2517, 31st AIAA Applied Aerodynamics Conference, San Diego, CA, 24 - 27 June 2013.

[12]Lefebvre, A. and Zha, G.-C. . Design of High Wing Loading Compact Electric Airplane Utilizing CoFlow Jet Flow Control. AIAA Paper 2015-0772, AIAA SciTech2015: 53nd Aerospace Sciences Meeting, Kissimmee, FL, 5-9 Jan 2015.

[13]G.-C. Zha, Y. Shen, and B. Wang. An improved low diffusion E-CUSP upwind scheme . Journal of Computer & Fluids, 48:214220, 2011.

[14]P.R. Spalart and S.R. Allmaras. A One-equation Turbulence Model for Aerodynamic Flows. AIAA-92- 0439, 1992.

[15]P. Roe. Approximate Riemann Solvers, Parameter Vectors, and Difference Schemes. Journal of Computational Physics, 43:357372, 1981.

[16]Shen, Y.-Q. and Zha, G.-C. and Wang, B.-Y. Improvement of Stability and Accuracy of Implicit WENO Scheme. AIAA Journal, 47, No. 2:331344, 2009.

[17]Shen, Y.-Q. and Zha, G.-C. and Chen, X.-Y. High Order Conservative Differencing for Viscous Terms and the Application to Vortex-Induced Vibration Flows. Journal of Computational Physics, 228(2):82838300, 2009.

[18]Y.-Q. Shen, B.-Y. Wang, and G.-C. Zha. Implicit WENO Scheme and High Order Viscous Formulas for Compressible Flows . AIAA Paper 2007-4431, 2007.

[19]B.-Y. Wang and G.-C. Zha. A General Sub-Domain Boundary Mapping Procedure For Structured Grid CFD Parallel Computation. AIAA Journal of Aerospace Computing, Information, and Communication, 5, No.11:20842091, 2008.

[20]Y.-Q. Shen and G.-C. Zha. Comparison of High Order Schemes for Large Eddy Simulation of Circular Cylinder Flow. AIAA-2009-0945, 47th AIAA Aerospace Sciences Meeting and Exhibit, Orlando, FL, Jan. 5-8, 2009.

[21]Y.-Q. Shen J.-Y. Gan and G.-C Zha. Comparison of Drag Prediction Using RANS models and DDES for the DLR-F6 Configuration Using High Order Schemes. 54th Aerospace Sciences Meeting, San Diego, CA, AIAA Paper 2016-0553, 2016.

[22]Wang, B. Y and Zha, G.-C. Detached-Eddy Simulation of a Co-Flow Jet Airfoil at High Angle of Attack. AIAA Journal of Aircraft, 48, 5:14951502, 2011.

[23]Im, H.-S. and Zha, G.-C. and Dano, B. P. E. Large Eddy Simulation of Coflow Jet Airfoil at High Angle of Attack. Journal of Fluid Engineering, 136(2):021101, 2014.

[24]G.-C Zha, B. Carroll, C. Paxton, A. Conley, and A. Wells. High Performance Airfoil with Co-Flow Jet Flow Control. AIAA-Paper-2005-1260, AIAA the 43rd Aerospace Sciences Meeting and Exhibit Conference, Reno, NV, Jan. 10-13, 2005.

[25]M. A. McDonald P. H. Cook and M. C. P. Firmin. AEROFOIL RAE 2822: PRESSURE DISTRIBUTIONS, AND BOUNDARY LAYER AND WAKE MEASUREMENTS. AGARD Advisory Report, 138-A6:177, 1979.